
Faculty of Engineering

Faculty Publications

Nanoplasmonics enhanced terahertz sources

Afshin Jooshesh, Levi Smith, Mostafa Masnadi-Shirazi, Vahid Bahrami-Yekta,
Thomas Tiedje, Thomas E. Darcie, and Reuven Gordon

November 2014

This article was originally published at:

<http://dx.doi.org/10.1364/OE.22.027992>

Citation for this paper:

Jooshesh, A., Smith, L., Masnadi-Shirazi, M., Bahrami-Yekta, V., Tiedje, T., Darcie, T.E. & Gordon, R. (2014). Nanoplasmonics enhanced terahertz sources. *Optics Express*, 22(23), 27992-28001.

Nanoplasmonics enhanced terahertz sources

Afshin Jooshesh,¹ Levi Smith,¹ Mostafa Masnadi-Shirazi,² Vahid Bahrami-Yekta,¹
Thomas Tiedje,¹ Thomas E. Darcie,¹ and Reuven Gordon^{1,*}

¹Department of Electrical and Computer Engineering, University of Victoria, 3800 Finnerty Road, Victoria, British Columbia V8P 5C2, Canada

²Department of Electrical and Computer Engineering, University of British Columbia, 2329 West Mall, Vancouver, British Columbia V6T 1Z4, Canada

*rgordon@uvic.ca

Abstract: Arrayed hexagonal metal nanostructures are used to maximize the local current density while providing effective thermal management at the nanoscale, thereby allowing for increased emission from photoconductive terahertz (THz) sources. The THz emission field amplitude was increased by 60% above that of a commercial THz photoconductive antenna, even though the hexagonal nanostructured device had 75% of the bias voltage. The arrayed hexagonal outperforms our previously investigated strip array nanoplasmonic structure by providing stronger localization of the current density near the metal surface with an operating bandwidth of 2.6 THz. This approach is promising to achieve efficient THz sources.

©2014 Optical Society of America

OCIS codes: (250.5403) Plasmonics; (160.5140) Photoconductive materials; (040.2235) Far infrared or terahertz.

References and links

1. P. U. Jepsen, R. H. Jacobsen, and S. R. Keiding, "Generation and detection of terahertz pulses from biased semiconductor antennas," *J. Opt. Soc. Am. B* **13**(11), 2424–2436 (1996).
2. D. Auston, K. Cheung, J. Valdmanis, and D. Kleinman, "Cherenkov Radiation from Femtosecond Optical Pulses in Electro-Optic Media," *Phys. Rev. Lett.* **53**(16), 1555–1558 (1984).
3. B. B. Hu and M. C. Nuss, "Imaging with terahertz waves," *Opt. Lett.* **20**(16), 1716–1718 (1995).
4. C. Jansen, S. Wietzke, O. Peters, M. Scheller, N. Vieweg, M. Salhi, N. Krumbholz, C. Jördens, T. Hochrein, and M. Koch, "Terahertz imaging: applications and perspectives," *Appl. Opt.* **49**(19), E48–E57 (2010).
5. P. U. Jepsen, D. G. Cooke, and M. Koch, "Terahertz spectroscopy and imaging - Modern techniques and applications," *Laser Photon. Rev.* **5**(1), 124–166 (2011).
6. Kasalynas, R. Venkevicius, and G. Valusis, "Continuous wave spectroscopic terahertz imaging with InGaAs bow-tie diodes at room temperature," *IEEE Sens. J.* **13**(1), 50–54 (2013).
7. K. Kawase, Y. Ogawa, Y. Watanabe, and H. Inoue, "Non-destructive terahertz imaging of illicit drugs using spectral fingerprints," *Opt. Express* **11**(20), 2549–2554 (2003).
8. D. M. Mittleman, M. Gupta, R. Neelamani, R. G. Baraniuk, J. V. Rudd, and M. Koch, "Recent advances in terahertz imaging," *Appl. Phys. B* **68**(6), 1085–1094 (1999).
9. K. Serita, S. Mizuno, H. Murakami, I. Kawayama, Y. Takahashi, M. Yoshimura, Y. Mori, J. Darmo, and M. Tonouchi, "Scanning laser terahertz near-field imaging system," *Opt. Express* **20**(12), 12959–12965 (2012).
10. Y. C. Shen, T. Lo, P. F. Taday, B. E. Cole, W. R. Tribe, and M. C. Kemp, "Detection and identification of explosives using terahertz pulsed spectroscopic imaging," *Appl. Phys. Lett.* **86**(24), 241116 (2005).
11. C. Yu, S. Fan, Y. Sun, and E. Pickwell-Macpherson, "The potential of terahertz imaging for cancer diagnosis: A review of investigations to date," *Quant. Imaging Med. Surg.* **2**(1), 33–45 (2012).
12. S. L. Dexheimer, *Terahertz Spectroscopy: Principles and Applications* (CRC, 2008).
13. R. Faulks, S. Rihani, H. E. Beere, M. J. Evans, D. A. Ritchie, and M. Pepper, "Pulsed terahertz time domain spectroscopy of vertically structured photoconductive antennas," *Appl. Phys. Lett.* **96**(8), 081106 (2010).
14. B. M. Fischer, M. Walther, and P. U. Jepsen, "Far-infrared vibrational modes of DNA components studied by terahertz time-domain spectroscopy," *Phys. Med. Biol.* **47**(21), 3807–3814 (2002).
15. S. Yu, B. J. Drouin, and J. C. Pearson, "Terahertz Spectroscopy of the Bending Vibrations of Acetylene12c2h2," *Astrophys. J.* **705**(1), 786–790 (2009).
16. M. Walther, D. Cooke, C. Sherstan, M. Hajar, M. Freeman, and F. Hegmann, "Terahertz conductivity of thin gold films at the metal-insulator percolation transition," *Phys. Rev. B* **76**(12), 125408 (2007).
17. B. Heshmat, M. Masnadi-Shirazi, R. B. Lewis, J. Zhang, T. Tiedje, R. Gordon, and T. E. Darcie, "Enhanced Terahertz Bandwidth and Power from GaAsBi-based Sources," *Adv. Opt. Mater.* **1**(10), 714–719 (2013).
18. B. Heshmat, H. Pahlevaninezhad, Y. Pang, M. Masnadi-Shirazi, R. Burton Lewis, T. Tiedje, R. Gordon, and T. E. Darcie, "Nanoplasmonic terahertz photoconductive switch on GaAs," *Nano Lett.* **12**(12), 6255–6259 (2012).

19. S. G. Park, K. H. Jin, M. Yi, J. C. Ye, J. Ahn, and K. H. Jeong, "Enhancement of terahertz pulse emission by optical nanoantenna," *ACS Nano* **6**(3), 2026–2031 (2012).
20. D. M. Mittleman, "Frontiers in terahertz sources and plasmonics," *Nat. Photonics* **7**(9), 666–669 (2013).
21. C. W. Berry, M. R. Hashemi, and M. Jarrahi, "Generation of high power pulsed terahertz radiation using a plasmonic photoconductive emitter array with logarithmic spiral antennas," *Appl. Phys. Lett.* **104**(8), 081122 (2014).
22. S. Jafarlou, M. Neshat, and S. Safavi-Naeini, "A hybrid analysis method for plasmonic enhanced terahertz photomixer sources," *Opt. Express* **21**(9), 11115–11124 (2013).
23. V. Pačebutas, K. Bertulis, L. Dapkus, G. Aleksejenko, A. Krotkus, K. M. Yu, and W. Walukiewicz, "Characterization of low-temperature molecular-beam-epitaxy grown GaBiAs layers," *Semicond. Sci. Technol.* **22**(7), 819–823 (2007).
24. V. Pačebutas, K. Bertulis, A. Bičiūnas, and A. Krotkus, "Low-temperature MBE-grown GaBiAs layers for terahertz optoelectronic applications," *Phys. Status Solidi* **6**(12), 2649–2651 (2009).
25. C. Baker, I. S. Gregory, W. R. Tribe, I. V. Bradley, M. J. Evans, E. H. Linfield, and M. Missous, "Highly resistive annealed low-temperature-grown InGaAs with sub-500," *Appl. Phys. Lett.* **85**(21), 4965 (2004).
26. M. Awad, M. Nagel, H. Kurz, J. Herfort, and K. Ploog, "Characterization of low temperature GaAs antenna array terahertz emitters," *Appl. Phys. Lett.* **91**(18), 181124 (2007).
27. J. Sigmund, C. Sydlo, H. L. Hartnagel, N. Benker, H. Fuess, F. Rutz, T. Kleine-Ostmann, and M. Koch, "Structure investigation of low-temperature-grown GaAsSb, a material for photoconductive terahertz antennas," *Appl. Phys. Lett.* **87**(25), 252103 (2005).
28. Kostakis, D. Saeedkia, and M. Missous, "Terahertz Generation and Detection Using Low Temperature Grown InGaAs-InAlAs Photoconductive Antennas at 1.55," *IEEE Trans. THz. Sci. Technol.* **2**(6), 617–622 (2012).
29. M. Mittendorff, M. Xu, R. J. Dietz, H. Künzel, B. Sartorius, H. Schneider, M. Helm, and S. Winnerl, "Large area photoconductive terahertz emitter for 1.55 μm excitation based on an InGaAs heterostructure," *Nanotechnology* **24**(21), 214007 (2013).
30. K. Moon, D. W. Park, I. M. Lee, N. Kim, H. Ko, S. P. Han, D. Lee, J. W. Park, S. K. Noh, and K. H. Park, "Low-temperature-grown InGaAs terahertz photomixer embedded in InP thermal spreading layer regrown by metalorganic chemical vapor deposition," *Opt. Lett.* **38**(24), 5466–5469 (2013).
31. S. Rihani, R. Faulks, H. E. Beere, I. Farrer, M. Evans, D. A. Ritchie, and M. Pepper, "Enhanced terahertz emission from a multilayered low temperature grown GaAs structure," *Appl. Phys. Lett.* **96**(9), 091101 (2010).
32. M. Tani, S. Matsuura, K. Sakai, and S.-i. Nakashima, "Emission characteristics of photoconductive antennas based on low-temperature-grown GaAs and semi-insulating GaAs," *Appl. Opt.* **36**(30), 7853–7859 (1997).
33. Y. Lee, *Principles of Terahertz Science and Technology* (Springer, 2009).
34. S. Preu, G. H. Döhler, S. Malzer, L. J. Wang, and A. C. Gossard, "Tunable, continuous-wave Terahertz photomixer sources and applications," *J. Appl. Phys.* **109**(6), 061301 (2011).
35. J. Y. Suen, W. Li, Z. D. Taylor, and E. R. Brown, "Characterization and modeling of a terahertz photoconductive switch," *Appl. Phys. Lett.* **96**(14), 141103 (2010).
36. L. Tian and W. Shi, "Analysis of operation mechanism of semi-insulating GaAs photoconductive semiconductor switches," *J. Appl. Phys.* **103**(12), 124512 (2008).
37. P. N. Melentiev, A. E. Afanasiev, A. A. Kuzin, A. S. Baturin, and V. I. Balykin, "Giant optical nonlinearity of a single plasmonic nanostructure," *Opt. Express* **21**(12), 13896–13905 (2013).
38. K. Wang, E. Schonbrun, P. Steinvurzel, and K. B. Crozier, "Trapping and rotating nanoparticles using a plasmonic nano-tweezer with an integrated heat sink," *Nat. Commun.* **2**, 469 (2011).
39. H. Aouani, J. Wenger, D. Gérard, H. Rigneault, E. Devaux, T. W. Ebbesen, F. Mahdavi, T. Xu, and S. Blair, "Crucial role of the adhesion layer on the plasmonic fluorescence enhancement," *ACS Nano* **3**(7), 2043–2048 (2009).
40. A. Singh, S. Pal, H. Surdi, S. S. Prabhu, V. Nanal, and R. G. Pillay, "Highly efficient and electrically robust carbon irradiated semi-insulating GaAs based photoconductive terahertz emitters," *Appl. Phys. Lett.* **104**(6), 063501 (2014).
41. T. Liu, M. Tani, M. Nakajima, M. Hangyo, and C. Pan, "Ultrabroadband terahertz field detection by photoconductive antennas based on multi-energy arsenic-ion-implanted GaAs and semi-insulating GaAs," *Appl. Phys. Lett.* **83**(7), 1322 (2003).
42. BATOP instruction manual, "Instruction manual and data sheet PCA-40-05-10-800-x", <http://www.batop.com/products/terahertz/photoconductive-antenna/photoconductive-antenna-800nm.html>.
43. T. Kampfrath, M. Battiato, P. Maldonado, G. Eilers, J. Nötzold, S. Mährlein, V. Zbarsky, F. Freimuth, Y. Mokrousov, S. Blügel, M. Wolf, I. Radu, P. M. Oppeneer, and M. Münzenberg, "Terahertz spin current pulses controlled by magnetic heterostructures," *Nat. Nanotechnol.* **8**(4), 256–260 (2013).
44. V. Apostolopoulos and M. E. Barnes, "THz emitters based on the photo-Dember effect," *J. Phys. D Appl. Phys.* **47**(37), 374002 (2014).
45. M. van Exter and D. R. Grischkowsky, "Characterization of an optoelectronic terahertz beam system," *IEEE Trans. Microw. Theory Tech.* **38**(11), 1684–1691 (1990).
46. E. Castro-Camus, J. Lloyd-Hughes, and M. Johnston, "Three-dimensional carrier-dynamics simulation of terahertz emission from photoconductive switches," *Phys. Rev. B* **71**(19), 195301 (2005).
47. K. Sala, G. Kenney-Wallace, and G. Hall, "CW autocorrelation measurements of picosecond laser pulses," *IEEE J. Quantum Electron.* **16**(9), 990–996 (1980).
48. C. A. Balanis, *Antenna Theory Analysis and Design* (John Wiley & Sons, Canada, 2005).
49. J. Krause, M. Wagner, S. Winnerl, M. Helm, and D. Stehr, "Tunable narrowband THz pulse generation in scalable large area photoconductive antennas," *Opt. Express* **19**(20), 19114–19121 (2011).

50. A. Krotkus, "Semiconductors for terahertz photonics applications," *J. Phys. D Appl. Phys.* **43**(27), 273001 (2010).
51. C. W. Berry, M. R. Hashemi, S. Preu, H. Lu, A. C. Gossard, and M. Jarrahi, "High power terahertz generation using 1550 nm plasmonic photomixers," *Appl. Phys. Lett.* **105**(1), 011121 (2014).
-

1. Introduction

A photoconductive antenna (PCA) can produce terahertz (THz) bandwidth pulses by the generation of photocarriers in the antenna gap using a femtosecond laser [1, 2]. Such THz waves (0.3–10 THz) have applications in security, imaging [3–11], near-field scanning microscopy and spectroscopy [12–16]. Today, PCAs are commercially available as THz sources, with compact size, low cost, and room temperature operation.

Previously, nanoplasmonic structures have been investigated to enhance the performance of THz detectors [17–19]. The main advantage of the nanoplasmonic structure for detection is to create a fast sweep out time, and thereby allow for the usage of a low-cost high-mobility long carrier lifetime substrate like semi-insulating GaAs [18, 20–22], as opposed to other less common substrates with short carrier lifetimes (such as low-temperature GaAs or GaBiAs) [23–31]. For pulsed THz sources, however, the carrier lifetime is not a limiting factor [32], yet nanoplasmonic structures can still provide an advantage, as we will investigate in this work.

To understand the advantage of nanoplasmonic structures for THz sources, we consider that the radiated THz field amplitude is proportional to photocurrent density $E_{THz} \propto \partial J(t)/\partial t$ with $J(t) = n(t)q\mu E(t)$, where $n(t)$ is photocarrier density as a function of time, q is the electron charge, μ is mobility, and $E(t)$ is the bias field [33]. It is desirable to maximize J to maximize the THz field generated; however, the bias field and charge density are limited by material breakdown, charge screening and thermal damage [1, 34–36]. Among these, the most significant factor is thermal damage. Many researchers in the nanoplasmonics community have realized the ability of metal nanostructures to effectively remove heat in high-field applications such as nonlinear optics [37] and optical tweezers [38]. Here we demonstrate that both the bias field and the carrier density can be increased in a nanoplasmonic structure by reducing heat generation and effectively removing heat generated near the metal nanostructures. Therefore, the main roles of the nanostructured metal are to localize the current density near the metal to reduce heat generation while maximizing THz emission and ensuring that the heat that is generated is efficiently removed.

2. Fabrication

Figure 1 shows the nanoplasmonic structures investigated in this work. We used a 500 μm SI-GaAs (100) wafer with 10 $\text{M}\Omega\cdot\text{cm}$ resistivity and electron mobility of $\sim 5500 \text{ cm}^2/\text{V}\cdot\text{s}$. Closed-gap dipole antennas were patterned using contact UV-photolithography on cleaved substrates. The samples were then placed in an e-beam evaporator to deposit 100 nm gold with a 5 nm titanium (Ti) adhesion layer. We used Ti instead of Cr to increase the electric field of the surface plasmons of the gold and semiconductor interface [39]. Finally, plasmonic structures were milled through the gold using a focused ion beam Hitachi FB-2100 at 11.6 pA current and 40 kV bias. Two 100 nm hexagonal array plasmonic samples, one 100 nm gap strip array plasmonic structure and a 5 μm gap dipole were fabricated for the experiment. The periodicity p and the apex angle θ of the hexagonal structure were optimized using FDTD to increase the field intensity in the substrate (see Appendix A).

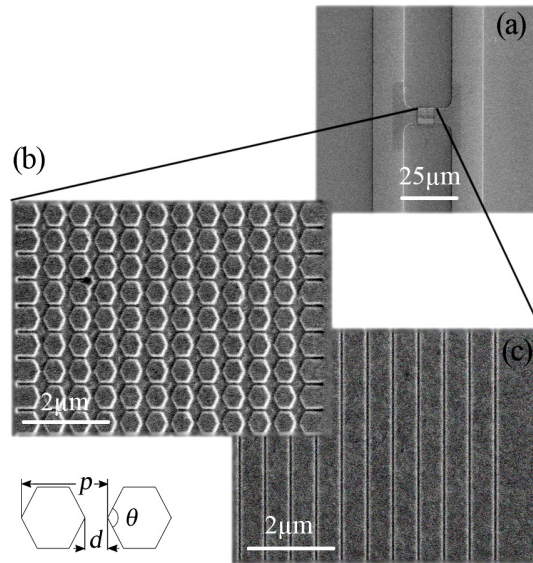


Fig. 1. a) Scanning electron microscope image of the 20 μm dipole on SI-GaAs substrate. b) The active area of the hexagonal plasmonic array. c) The active area of the strip plasmonic array. The diagram shows apex angle θ , gap size d and periodicity p .

Figure 2(a) shows the PCA testing setup. Samples were mounted on a printed board circuit (PCB) and positioned against a high resistivity float zone silicon aspheric focusing lens with focal length of 53 mm. The femtosecond-laser is a 785 nm mode-locked fiber laser, which generates 100 fs optical pulses with a 68.9 MHz repetition rate. The delay line was used to sample a 100 ps time window of the THz pulse. In this setup, transmitters were biased with a chopped voltage and illuminated with an average 10 mW of optical power. A commercial BATOP (PCA-40-05-10-800-a) photoconductive antenna was placed as a receiver during the measurements at the distance of 10.6 mm from the transmitter with an average 13 mW of optical power. A lock-in amplifier (Stanford SR830) was used to measure the current at the receiver, which is proportional to the THz field.

3. Results and discussion

The time domain response and power spectra are shown in Figs. 2(b) and 2(c). Clearly, the 100 nm hexagonal array has the highest intensity and bandwidth.

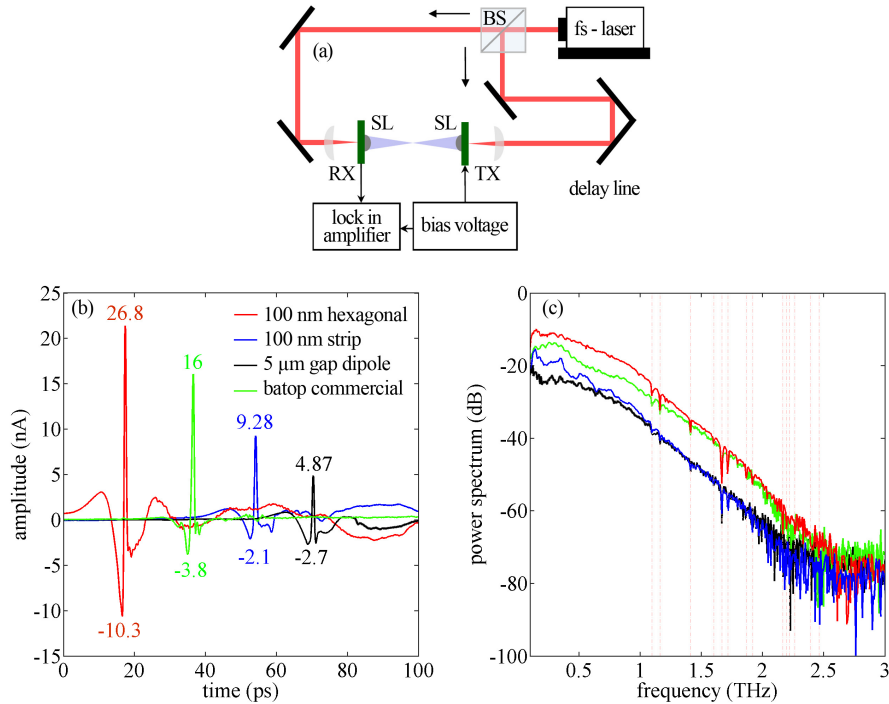


Fig. 2. a) Pulsed mode terahertz setup. BS is a Beam splitter, SL is silicon lens, TX is the transmitter PCA and RX is the commercial PCA receiver. b) and c) are received time and frequency domain signals. Red line is the response of the hexagonal array device resulting in 32 nA peak-to-peak current amplitude, blue line is the strip array device with 11.38 nA peak-to-peak current, green line is the Batop commercial device as a transmitter with 19.8 nA peak-to-peak current and black line is the received THz signal of a 5 μm gap dipole with 7.57 nA peak-to-peak current. Dashed lines in c) are HITRAN water absorption lines.

The higher intensity in Fig. 2(b) is directly proportional to the photocurrent. The maximum photocurrent is limited by the bias that can be achieved prior to thermally induced breakdown. To determine the bias, we measured the I-V characteristics under illumination, as shown in Fig. 3. Using the results from Fig. 3, the bias was set to 20% of the on-set of breakdown, to be consistent with the operating characteristics of the commercial sample. Even though the voltage is higher for the 5 μm gap structure, the local bias field is higher in the nanoplasmonic structures, due to the smaller gaps. Also, the hexagonal array structure has apices that further act to confine the bias field, and thereby increase the local current density. We note that there is an offset in the I-V characteristic due to photocurrent which is not present under dark conditions (see Appendix B). The observed nonlinear rise in current at higher biases is commonly found in THz devices and it comes from Ohmic heating (e.g., see [40, 41]). This limits practical device operation to values below the nonlinear regime [42]. The heat generation is represented by the product of current and voltage in Fig. 3. Clearly from this, the hexagonal structure has less heating at its operation point (10 V) than the 5 μm gap dipole at its operation point (20 V) since the current voltage product is lower.

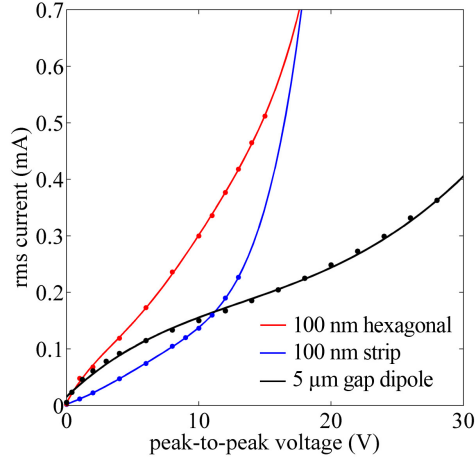


Fig. 3. Electrical characteristics of our semi-insulating GaAs based samples under laser illumination.

Figure 4(a) shows the THz power as a function of femtosecond laser average power, which generates the photocarriers. Comparing the hexagonal and strip array, we see that the initial slope in the THz power generated is higher for the hexagonal array structure, even for the same bias voltage of 10 V used here. This is due to a combination of the higher local bias field and the localization of the photocarriers near the apexes. Of course, screening plays a bigger role in the hexagonal array structure due to the larger photocarrier density, which can be seen from the saturation in the enhancement factor when normalizing to the 5 micron gap, as shown in Fig. 4(b).

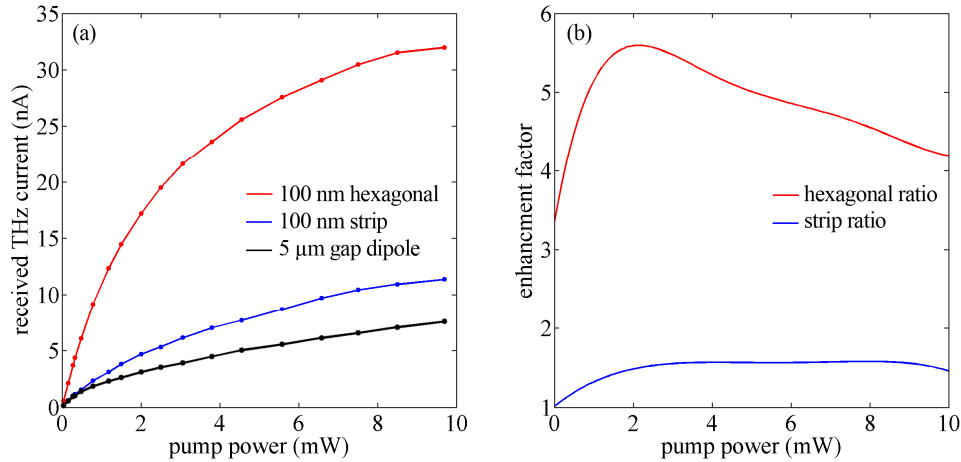


Fig. 4. a) Peak THz received current of the samples with pump power. b) Enhancement ratio with respect to 5 μm gap dipole ($I_{\text{plasmonic}}/I_{5 \mu\text{m gap}}$).

As mentioned previously, the improvements to performance are related to the increased photocurrent that can be achieved, due to increased local bias field and photocarriers generated. Gold has a thermal conductivity ($3.14 \text{ W/cm}\cdot\text{K}$) that is 6 times that of GaAs ($0.55 \text{ W/cm}\cdot\text{K}$). The current density is localized underneath the gold edges for the nanoplasmonic structures, so this benefits efficient heat removal. We can tell from the experiments that the hexagonal nanoplasmonic structure is removing heat more effectively because the THz generation is higher for a given photocurrent. The photocurrent in the 5 μm gap structure is comparable in Fig. 3 at the respective bias points (10 V for the hexagonal structure, 10 V for the strip structure and 20 V for the gap structure), but THz generation is much less in Fig. 4.

This shows that a significant portion of the current in the 5 μm gap structure is from thermally generated carriers after the optical pulse and does not contribute to THz generation. These thermally generated carriers appear because the heat is not effectively removed from the 5 μm gap structure.

In this work, the THz emission is enhanced in a biased configuration due to improved thermal management associated with the nanoplasmonic structures. More generally, such thermal management strategies may also benefit unbiased devices based on asymmetric transport [43, 44], insofar as transport properties are thermally dependent and ultimately devices will fail mechanically under excessive thermal load.

We use numerical simulation to quantify local current density in the various structures investigated and relate this to the experimental observations. In Table 1, we consider the photocurrent enhancement by integrating the bias field times the laser power in the GaAs (which is proportional to the photocarriers generated) as determined by finite-difference time-domain simulations (see Appendix C for details): $\eta = \int E \cdot P dv$. We see that the hexagonal array nanoplasmonic structure has the highest enhancement. If we multiply these by the experimentally used voltage, we see reasonable quantitative agreement with our experimentally measured peak THz field, to within a constant scaling factor ($C = 0.93$) dependent on the experimental setup. We have neglected screening in this analysis, which has a bigger influence on the hexagonal structures, as described above. This can explain the lower measured current for the hexagonal structure as compared with the numerical prediction. This table shows that we can obtain higher generation from the hexagonal nanoplasmonic structure at the thermally limited operation point.

Table 1. Theoretical and measured emission amplitudes of plasmonic photoconductive antennas.

gap structure	η	bias (V)	$I_{\text{THz}} = \eta \times C \times V$ (a.u.)	measured I_{THz} (nA)
hexagonal	4.26	10	39.6	32
strip	1.13	10	10.51	11.38
5 μm gap	0.29	20	5.39	7.57

The bandwidth obtained is comparable for all devices and similar to past works [26, 45, 46]. We have used a short dipole to give a more uniform emission pattern than our past work [18]. We have confirmed via CST simulations with a discrete port source in the center of the dipole (not shown) that the THz emission pattern and amplitude are not affected significantly by the plasmonic structures. This is because all the features are much smaller than the THz wavelength (~ 100 microns). To study the bandwidth, we estimated the RC time constant of around 0.5 fs (see Appendix D for details), and this is not a limiting factor in the bandwidth. In theory, a 100 fs Gaussian pulse corresponds to 4.4 THz bandwidth [47]. The radiation amplitude of a small dipole scales with $I(f)^2 f^2$ where $I(f)$ is the frequency dependent photocurrent and f is the frequency [48]. While the f^2 has a high-pass effect, other factors typically [1, 49, 50] cause the THz generation to fall off at higher frequencies. For example, the spectrum of the current follows the envelope of the optical pulse [33], which decays rapidly at higher frequencies. Furthermore, the high frequency response is reduced by kinetic inductance (see Appendix D for details).

4. Conclusion

In conclusion, we have demonstrated that nanoplasmonic structures can be used to improve the performance of THz photoconductive sources. Nanoscale localization of the bias field and carrier density close to the metal surface allows for rapid removal of heat, which typically limits PCA power output. In the future, we hope to expand these thermal-management strategies to improve the performance of CW photomixers, where there have already been pioneering works using nanoplasmonics, but not focusing on the thermal management aspects [51].

Appendix A: Optimization of hexagonal array nanoplasmonic structure with finite-difference time-domain simulations

We used the particle swarm optimization method implemented in Lumerical FDTD with the goal of maximizing the transmission into the substrate. Johnson & Christy permittivity values were used for gold. Since the saturation velocity of electrons in GaAs is 1.2×10^7 cm/s, a 100 nm gap is considered to allow electrons to reach the electrodes in sub-picosecond time. Therefore, with a fixed 100 nm gap size, we varied the 2-dimensional periodicity of the gold from 400 nm to 800 nm and the apex angle θ between 90° and 180° . We found that periodicity of 587 nm with $\theta=127^\circ$ results in maximum transmission into the substrate with a source at 785 nm wavelength.

Figure 5(a) shows 2D optical power density profile of a single hexagonal cell with 100 nm gap size excited at 785 nm. A cross section view of the hexagonal plasmonic cells in Fig. 5(b) shows a higher power density profile beneath the hexagon apexes, as compared with a strip array plasmonic structure shown in Fig. 5(c). Therefore, we expect to generate a greater number of carriers close to the apexes of the hexagonal array nanostructures.

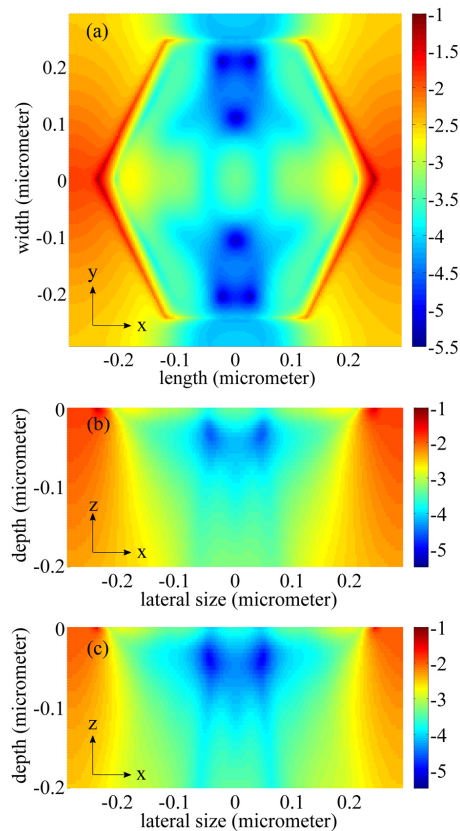


Fig. 5. FDTD simulation results for $\log_{10}(|P|)$ at 785 nm and in an arbitrary scale. a) 2D surface power density profile of a single cell period from top, b) cross section view of a single hexagonal cell with 100 nm gap distance, c) cross section view of a 100 nm strip plasmonic structure.

Appendix B: Electrical characteristics of the in-house fabricated samples

Figure 6 shows the dark (without illumination) current-voltage characteristic of the photoconductive switches. Thermally generated carriers lead to the dark current, which has a nonlinear behavior (seen in our fitting) as Ohmic heating leads to more thermal carrier

generation. This dark current is typically much lower than the photocurrent (see Fig. 3); however, thermal effects still play a role at higher biases under illuminated conditions.

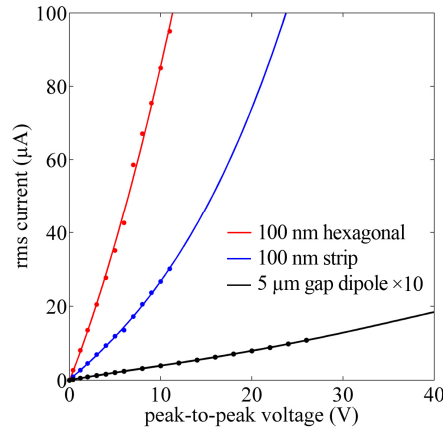


Fig. 6. Electrical characteristics of photoconductive switches in dark.

Appendix C: Photocurrent enhancement

A key factor in determining the radiation efficiency of the photoconductive emitters is the photocurrent that is generated during the absorption of the pump. As explained in the manuscript, the hexagon structure confines both electric bias field and laser power into the area between apexes. Because the number of photo-generated carriers is proportional to the power inside the gap we can rewrite the current density as $J \propto P \cdot E$ where P and E are the power at 785 nm and the bias electric field distribution profiles inside the gap. We used a plain wave source in FDTD at 0.5 THz (a nominal low frequency value) to determine the quasi-static electric field profile in a 3-dimensional unit cell ($587 \text{ nm} \times 587 \text{ nm} \times 400 \text{ nm}$ depth) of the plasmonic structures. Then, we normalized the electric field to the voltage drop over each cell of the array according to experimental conditions. Similarly the power profile of a 3-dimensional unit cell was obtained by FDTD simulations using a source at 785 nm. The product of P and E provides the current density distribution at each point. After integrating the $P \cdot E$ over YZ plane slices, the current profile can be plotted over the X axis as can be seen in Fig. 7. Finally, the photocurrent enhancement $\eta = \int E \cdot P dv$ obtained by integrating over the gap area along the X axes.

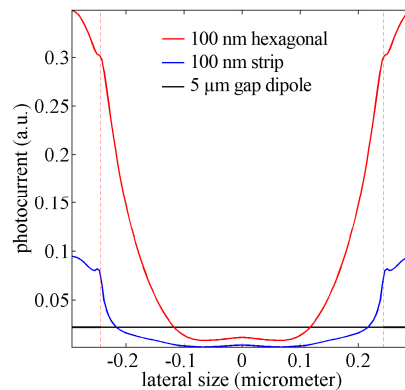


Fig. 7. FDTD simulation results for the photocurrent (P.E) over a unit cell of the plasmonic structures inside the SI-GaAs substrate. Red line is the photocurrent of the hexagonal structure. Blue line is the photocurrent of the strip structure and black is the photocurrent of the GaAs without plasmonic structures on the surface.

Appendix D: Capacitive time constant of the structure

We found a resistivity of 0.5Ω for the hexagonal array plasmonic structure, 1.2Ω for the strip array plasmonic structure and 27Ω for the $5 \mu\text{m}$ gap photoconductive antenna, using their current-voltage characteristics. Electrostatic simulations in COMSOL Multiphysics suggest a capacitance between 1 fF to 1.5 fF for the plasmonic and $5 \mu\text{m}$ gap dipole that gives a resistance-capacitance time constant of around 0.5 fs . Therefore, we believe that the RC-roll off does not limit the bandwidth of the THz pulse.

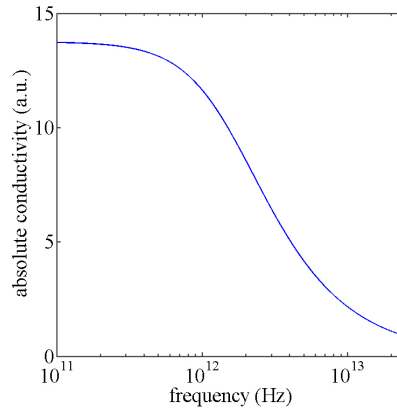


Fig. 8. Conductivity response of GaAs as a function of frequency.

As shown in Fig. 8, the Drude complex conductivity model shows a notable drop in conductivity at THz frequencies, which reduces the current as frequency increases (we considered a carrier momentum relaxation-time of 100 fs , as is common for semiconductors [50]).

Acknowledgment

The authors acknowledge funding from Natural Sciences and Engineering Research Council (NSERC) Canada Strategic Project Grant and Discovery Grant programs. The authors declare that there are no competing financial interests.